Journal of Materials Chemistry A

PAPER

View Article Online
View Journal | View Issue

Cite this: J. Mater. Chem. A, 2017, 5, 13785

Compositional control of precipitate precursors for lithium-ion battery active materials: role of solution equilibrium and precipitation rate†

Hongxu Dong and Gary M. Koenig Jr*

Received 27th April 2017
Accepted 13th June 2017

DOI: 10.1039/c7ta03653a

rsc.li/materials-a

Multicomponent transition metal oxides are among the most successful lithium-ion battery cathode materials, and many previous reports have described the sensitivity of final electrochemical performance of the active materials to the detailed composition and processing. Coprecipitation of a precursor template is a popular, scalable route to synthesize these transition metal oxide cathode materials because of the homogeneous mixing of the transition metals within the particles, and the morphology control provided by the precursors. However, the deviation of the precursor composition from feed conditions is a challenge that has generally not been reported in previous studies. Using a target final material of the high voltage spinel $LiMn_{1.5}Ni_{0.5}O_4$ as an example, we show in this study that the compositional deviation caused by coprecipitation can be significant under certain conditions, impacting the calcined final material structure and electrochemical properties. The study herein provides insights into the role of solution equilibrium and rate of precipitation of the transition metals during precipitate formation on precursor, and thus final active material, composition. Such knowledge is necessary to rationally predict and tune multicomponent battery precursor compositions synthesized *via* coprecipitation with high levels of accuracy.

Introduction

Due to their high energy density, lithium-ion (Li-ion) batteries have become a popular choice for applications ranging in scale from consumer electronics to electric vehicles to stationary energy storage systems.[1] Especially with regards to cathode materials, Li-ion batteries do not have a single material structure or composition that dominates but have many different materials that may be suited to a particular performance or cost objective.[2–15] Many current and future commercial cathode materials are multicomponent transition metal (TM) oxides including $LiNi_{0.80}Co_{0.15}Al_{0.05}O_2$,[7,18–22] $LiNi_{1/3}Mn_{1/3}Co_{1/3}O_2$,[14–17] $LiNi_{0.5}Mn_{0.5}O_2$,[36–38] $LiMn_{1.5}Ni_{0.5}O_4$,[7,23–34] and $xLiMn_2O_3(1-x)LiNi_{1/3}Mn_{1/3}Co_{1/3}O_2$.[8,39–42] Such materials have been reported to have material structure and electrochemical performance that is highly sensitive to the stoichiometry of the final material.

Various routes have been reported in the literature to synthesize multicomponent metal oxide cathode materials, including direct solid-state conversion of individual precursors,[43–49] hydrothermal synthesis,[50–53] spray pyrolysis,[54–58] and various deposition techniques.[59–62] One method that is very popular in the literature is coprecipitation of precursors followed by calcination to final active materials. Coprecipitation has the advantages that it is relatively easy to perform in the lab, scalable, allows tunable and monodisperse particle morphologies,[19,63–70] and provides homogeneous mixing of the multiple TM components throughout the secondary particles. While coprecipitation has many advantages and there are many reports synthesizing high performance materials using this method, one common assumption of materials produced *via* coprecipitation is that the particles retain the stoichiometry of the feed solution. However, depending on solution conditions this may not be a reasonable assumption. van Bommel *et al.* previously showed through equilibrium calculations that the fractions of Ni, Mn, and Co that remained as soluble species during hydroxide coprecipitation with a chelating agent were highly variable and pH dependent.[71] While these results suggest that predictive calculations should be done to adjust the feed stoichiometry to target the desired precipitate stoichiometry, the use of such analysis has rarely been reported. Many reports of multicomponent TM battery active materials that used coprecipitation of precursors for the final active material do not confirm the stoichiometry of the TMs in the precipitate. If calculations were performed, generally only solution equilibrium was considered; and the calculations were not used to guide decisions on precursor solution feed conditions. Also, no reports have considered whether the relative rate of coprecipitation varied for the different TMs. In this paper, a technique for

Department of Chemical Engineering, University of Virginia, 102 Engineers Way, Charlottesville, VA 22904-4741, USA. E-mail: gary.koenig@virginia.edu; Fax: +1-434-982-2658; Tel: +1-434-982-2714

† Electronic supplementary information (ESI) available. See DOI: 10.1039/c7ta03653a

determining the extent of coprecipitation of each TM independently in solution during synthesis will be described. Rates of coprecipitation from these measurements were used in combination with equilibrium calculations to achieve the goal of explicit composition control. We will demonstrate the impact of such control on material structural and electrochemical properties using an exemplar cathode material.

For this study, we have chosen the target cathode material $LiMn_{1.5}Ni_{0.5}O_4$ (LMNO), and to produce the material an oxalate precursor ($Mn_{0.75}Ni_{0.25}C_2O_4 \cdot 2H_2O$) was synthesized *via* coprecipitation with a 3 : 1 target Mn : Ni ratio. LMNO has a high operating voltage of 4.7 V *vs.* Li, and the power and energy density advantages have made LMNO a good candidate as the cathode active material for transportation and energy storage.[33,35,72–77] The sensitivity of LMNO material properties to TM stoichiometry,[67,78] coupled with the material having only two TM cations to consider, made this material an ideal candidate for this initial study.

We have chosen oxalate coprecipitation chemistry for LMNO synthesis because in isolation both Mn and Ni form stable oxalate dihydrate precipitates in aqueous solutions exposed to air, and oxalates have been previously used as battery precursors.[63,66,69,70,79] Carbonate coprecipitation is another popular method to synthesize 3 : 1 Mn : Ni precursor; however, $NiCO_3$ is difficult to form as a stable precipitate.[80–85] Hydroxide coprecipitation is more complex because of the tendency of Mn to oxidize to MnOOH.[70,71,87–91] Moreover, oxalate ions in the solution play a dual role as both the precipitation reagent and a complexing agent.[92–94] The formation of metal complexes with oxalate ions as the ligand slows down the precipitation rate and thus the nucleation and particle growth process becomes more controllable. According to previous reports, oxalate coprecipitation can be used to synthesize precursor particles of narrow size distribution, and particle morphologies were successfully tuned by careful control over solution conditions.[64,95] Explicit control over particle morphology can be important for battery active materials due to the role that morphology plays in electrode packing, electrode microstructure, and active material transport limitations.[26,96–101] However, synthesis that incorporates morphology control of precursor is often performed at low feed reagent concentrations where equilibrium and rate of precipitation need to be carefully considered and predefined. For the particular Mn–Ni blend oxalate coprecipitation reaction, previous reports have even explicitly noted adjustment of TM feed ratios using an empirical approach to compensate for the composition deviation.[102]

Equilibrium calculations in this study will show that feed stoichiometry can deviate significantly from the precipitate stoichiometry, and thus resulting final material composition. In addition, we will demonstrate that rate of precipitation of TMs needs to be considered, though experimental evidence will suggest the formation of seeds of the faster forming precipitate likely mitigates the impact of different rates of precipitation under some solution conditions. The techniques in this report should be translatable to other precursor systems such as hydroxides and carbonates.

Results and discussion

Concentration influence on deviation between actual and feed ratios

At equilibrium, stoichiometry deviations of the solid precipitates relative to the stoichiometry ratio of the feed solutions is primarily a result of the solubility differences between the TMs.[64,103] As will be shown later, all TMs in this study precipitate as oxalate dihydrates. At room temperature the solubility of $NiC_2O_4 \cdot 2H_2O$ is 0.0018 g/100 g water, whereas $MnC_2O_4 \cdot 2H_2O$ solubility is significantly greater at 0.0309 g/100 g water.[64] This solubility difference between $MnC_2O_4 \cdot 2H_2O$ and $NiC_2O_4 \cdot 2H_2O$ leads to the prediction that during a coprecipitation of a blend of Mn and Ni using oxalate the precipitate would be relatively enriched in Ni.[102] The proportional deviation from stoichiometry of the precipitate would be expected to become more significant as the total solution concentration of the TMs and oxalate is decreased, because the solubility limit would have a greater relative impact at lower concentrations. Fig. 1 displays the calculated Mn : Ni ratios in the precipitates at equilibrium as a function of total feed concentrations. Note that these are detailed calculations with many solution species at 60 °C, and not a result of only using the TM oxalate solubility values. Tabulated values are also listed in Table S1.† In all cases the Mn : Ni feed solution ratio was 3 : 1 and the TM : oxalate ratio was 1 : 1, and if all of the TM were to precipitate as oxalate the 3 : 1 ratio would be retained. It is observed that the Mn : Ni ratio drops sharply away from the 3 : 1 feed ratio as the total feed concentration decreases below 50 mM. The calculated ratio is 1.7 at 10 mM, which is nearly a 50% deviation from the feed ratio. Fig. 1 also contains the experimentally measured Mn : Ni ratios of the collected precursor powders determined by digesting the powders and using ICP analysis. All the precursors were collected 30 minutes after the TM and oxalate solutions were mixed together at 60 °C. In comparison to equilibrium

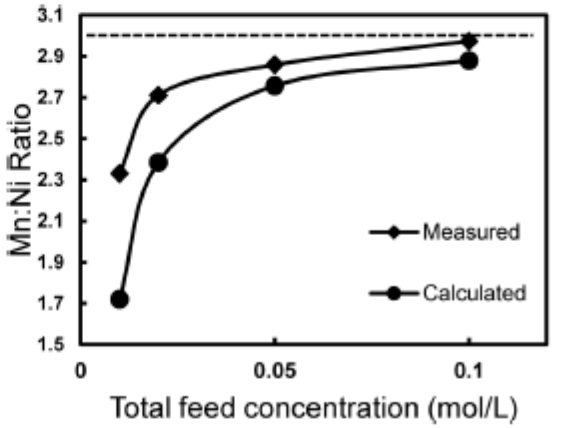

Fig. 1 The measured (diamonds) and calculated at equilibrium (circles) Mn : Ni stoichiometric ratio in the precipitate as a function of total TM feed concentration. The feed ratio of Mn : Ni is 3 : 1 in all cases, and a dashed line is added at Mn : Ni = 3.0 for comparison. Lines between data points added to guide the eye.

calculations, all the measured ratios are higher and closer to the feed ratio; and the gap increases as the total feed concentration decreases. As will be discussed later, our experiments suggest that this gap reflects the differences in the rate of precipitation of the Mn relative to Ni. As the concentration increases, the difference between the measured values and the calculated values decreases because the solution moves closer to equilibrium conditions faster with the rate of precipitation increasing at higher initial solution concentrations.

Precipitation timescales for pure and blend systems

The differences between equilibrium calculations and measured stoichiometries for the oxalate precipitates led to investigations of the concentration of the TM left in solution as a function of time. Before determining the concentration profile for the 3 : 1 Mn : Ni feed, first experiments were conducted with solutions containing only pure Mn or Ni at 20 mM. We chose to use 20 mM total TM (and oxalate) as the initial feed concentration for these experiments because (1) the concentration was low enough that it resulted in significant deviation between the equilibrium calculated and measured precipitate ratios (Fig. 1), and (2) this concentration was high enough to provide adequate amounts of precipitate powder for lithiation and calcination to final battery active material as well as materials characterization. Fig. 2a shows the concentration of soluble Mn as a function of time during coprecipitation of $MnC_2O_4 \cdot 2H_2O$. Fig. 2b shows the results of the same experiment where the only difference was the substitution of Mn with Ni. The soluble Mn concentration decreased faster than Ni for the pure TM experiments, indicating that pure $MnC_2O_4 \cdot 2H_2O$ initially precipitated faster than pure $NiC_2O_4 \cdot 2H_2O$. These results indicated that the manganese coprecipitation reaction had a lower activation barrier, resulting in $MnC_2O_4 \cdot 2H_2O$ crystallizing and precipitating faster than $NiC_2O_4 \cdot 2H_2O$ at the early nucleation stages. As discussed earlier, initial coprecipitation experiments were 30 minutes. The concentration of residual TM in the pure Ni experiment has not plateaued in this time frame, indicating that 30 minutes was not a sufficient timescale to approach equilibrium. We also note that while the pure Mn concentration appears to have reached a plateau in less than 30 minutes, the residual concentration still exceeds equilibrium (0.0045 mol L^{-1} compared to 0.0036 mol L^{-1}). SEMs of the resulting $MnC_2O_4 \cdot 2H_2O$ and $NiC_2O_4 \cdot 2H_2O$ precipitates collected after 30 minutes can be found in ESI, Fig. S1.† The faster precipitating

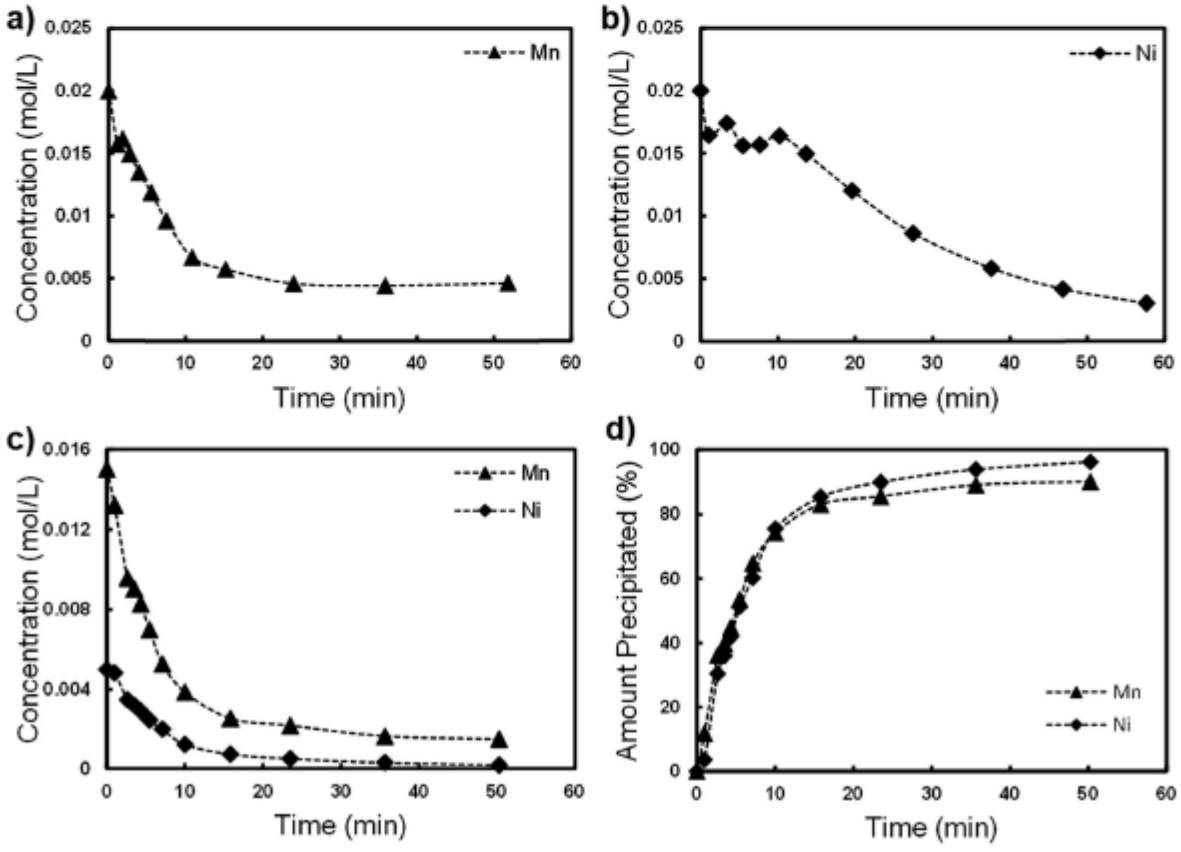

Fig. 2 Residual soluble (a) Mn and (b) Ni in solution during coprecipitation of pure $MnC_2O_4 \cdot 2H_2O$ and $NiC_2O_4 \cdot 2H_2O$. (c) Residual soluble Mn (triangles) and Ni (diamonds) during coprecipitation of feed with 3 : 1 Mn : Ni ratio. The total concentrations of TM and oxalate at the beginning of the coprecipitation for all solutions were 20 mM. (d) Fraction of Mn and Ni ions in precipitate. Dashed lines added to guide the eye.

$MnC_2O_4 \cdot 2H_2O$ particles were larger and had rougher surfaces than the $NiC_2O_4 \cdot 2H_2O$ material.

Although $MnC_2O_4 \cdot 2H_2O$ initially precipitated faster, after a sufficient time period (40 minutes), the soluble Ni concentration was significantly lower than the soluble Mn concentration. At long times, the precipitation of $NiC_2O_4 \cdot 2H_2O$ was more complete, consistent with the solubilities of the two TM oxalates. Based on the extent of coprecipitation measured for the two pure TM oxalate systems, the precipitate collected from the blend precipitation after 30 minutes would be expected to be relatively enriched in Mn; however, the opposite Mn-lean precipitate was observed experimentally (Fig. 1). These results indicated that there were additional considerations when Mn and Ni were coprecipitated from the same solution. Another interesting outcome from the experiments in Fig. 2a and b is that if the TMs precipitate at different rates, the resulting precursor would not be expected to be homogenous with regards to TM distribution in the precursor, which is a commonly cited advantage of coprecipitation synthesis for battery precursor materials. The pure Mn and Ni coprecipitation data suggests a Mn-rich core and Ni-rich shell, or separately Mn-rich and then Ni-rich precipitate particles, would likely result. To gain further insights, we conducted the same residual concentration as a function of time analysis for both Mn and Ni during the coprecipitation of a 3 : 1 Mn : Ni feed.

Fig. 2c displays the residual soluble Ni and Mn during precipitation of a feed 20 mM 3 : 1 Mn : Ni TM solution. Due to the difference in initial concentration of Ni and Mn, Fig. 2d shows the extent of Ni and Mn precipitated as a function of time, which is more instructive for comparing the homogeneity of the coprecipitation. Interestingly, in this synthesis with the blended TM feed both species precipitate at a nearly 1 : 1 ratio throughout the synthesis, contrary to expectations based on the pure Mn and Ni precipitation experiments. This implies an interaction between the two TMs and/or the TMs and the oxalate precipitates were facilitating this process. The precipitation of Ni in the 3 : 1 blend feed solution proceeds much faster than for the pure Ni feed, even though the 3 : 1 blend has the same total TM and oxalate concentration and lower Ni concentration. The blend coprecipitation resulted in higher overall extent of precipitation for both species after 30 minutes. Quantitatively, 87% of manganese ion and 92% of nickel ion precipitated, compared to 77% and 60% in their pure oxalate precipitation reactions, respectively. The resulting precipitate was now Ni-rich, which was consistent with previous observations (Fig. 1). These results led us to speculate that the faster-forming $MnC_2O_4 \cdot 2H_2O$ particles were providing seeds in the blend system to facilitate $NiC_2O_4 \cdot 2H_2O$ coprecipitation. To provide support for this speculation, we then conducted seeding experiments by adding 0.34 g of pure $MnC_2O_4 \cdot 2H_2O$ seeds at the beginning of a coprecipitation of 20 mM pure Ni^{2+} with oxalate (identical conditions to Fig. 2b except for seed addition). The mass of the seeds was chosen such that the amount of Mn atoms were 10% of the Ni atoms in the solution. Residual soluble nickel as a function of time during coprecipitation of pure Ni, pure Ni with $MnC_2O_4 \cdot 2H_2O$ seeds, and the Mn : Ni 3 : 1 system are shown in Fig. 3a. Fig. 3b is the fraction of Ni that has been precipitated as a function of time for the same experiments. It can be seen from Fig. 3a that adding $MnC_2O_4 \cdot 2H_2O$ seeds facilitated faster coprecipitation of nickel. However, inspection of Fig. 3b reveals that the coprecipitation of Ni in the seeded experiment was still slower than for the Mn : Ni 3 : 1 blend. We speculate that this difference was largely due to differences in surface area between the initial particles in the 3 : 1 blend synthesis and the $MnC_2O_4 \cdot 2H_2O$ particles in the seeded experiment. We expect that the initial precipitates that formed in the 3 : 1 blend synthesis were very small, though detailed characterization of their size was challenging and is a focus of current investigations in our lab. In contrast, the seed particles were from pure $MnC_2O_4 \cdot 2H_2O$ synthesis experiments and these particles were quite large, with an average size of ~20 μm that was consistent with previous reports.[39,68,104] A SEM image of the seeds can be found in ESI, Fig. S1.† The smaller particles that form *in situ* during synthesis in the 3 : 1 blend system provide more surface for the coprecipitation, speeding up the loss of residual Ni in the solution to the precipitate phase relative to the lower surface area seeded experiments. In summary, the seeded precipitation experiments provided

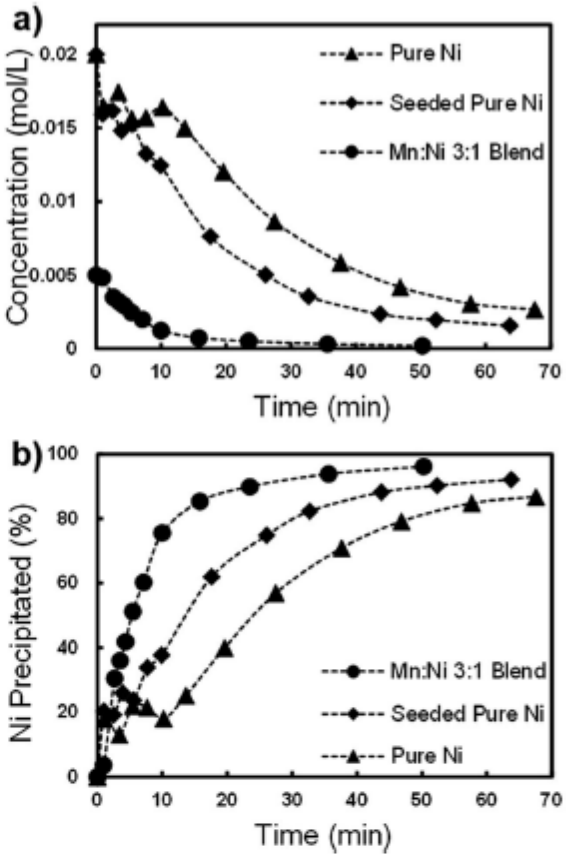

Fig. 3 (a) Measured soluble Ni as a function of time during coprecipitation of 20 mM oxalate with 20 mM Ni (triangles), 20 mM Ni with $MnC_2O_4 \cdot 2H_2O$ seeds (diamonds), and 20 mM 3 : 1 Mn : Ni (circles). (b) The fraction of Ni lost to the precipitate phase using the data in (a). Dashed lines added to guide the eye.

evidence that the $MnC_2O_4 \cdot 2H_2O$ in the 3 : 1 blend facilitates faster initial precipitate formation, which speeds up the precipitation of $NiC_2O_4 \cdot 2H_2O$. These results indicated that at least in some cases TMs with very different precipitation rates can precipitate almost at the same rate in blends because seeds of faster forming precipitates will facilitate increasing the precipitation rate of the slower precipitation compounds. Further investigation is needed to determine how general this observation is with regards to concentration regimes, TM species, and coprecipitation anions; however, it provides evidence that coprecipitation does indeed provide homogeneous TM precipitates – even if the rates of precipitation are quite different.

Oxalates structural and thermal characterization

According to previous reports, both Mn and Ni oxalates may exist in an α-phase dihydrate oxalate[94,105] whose prototype is the mineral humbodtine α-$FeC_2O_4 \cdot 2H_2O$ with monoclinic space group $C2/c$.[92] Nickel oxalate dihydrates have also been reported to crystallize in the orthorhombic system in space group $Cccm$,[94,105] whose X-ray peaks are indexed with β-$FeC_2O_4 \cdot 2H_2O$.[92] Mn oxalate, unlike the other d-block TM oxalates, does not present an orthorhombic β-$M^{II}C_2O_4 \cdot 2H_2O$ (where M stands for the d-block TM) modification.[94,105] It has another dihydrate, however, denominated as γ-$MnC_2O_4 \cdot 2H_2O$ which is also orthorhombic while belonging to space group $P2_12_12_1$ and is found to crystallize under high pH conditions.[68]

XRD patterns of the pure and blend TM oxalate powders were analysed to determine the resulting structures (Fig. 4). The pure Mn oxalate was indexed with the α-$FeC_2O_4 \cdot 2H_2O$ monoclinic phase and the pure Ni oxalate was indexed with the β-$FeC_2O_4 \cdot 2H_2O$ orthorhombic phase.[92] The XRD pattern of the blend 3 : 1 feed TM oxalate (note: ICP composition was 2.6 : 1 Mn : Ni) powder was identical to the pattern of Ni oxalate powder, consistent with the β-oxalate, rather than a co-existence of the two oxalate polymorphs. The peaks in the blend oxalate, however, are less sharp and intense compared to the pure Ni oxalate dihydrate, which indicates some non-ideal mixing of the cations in the lattice structure and/or smaller crystallite sizes.[92] The peaks of the blend powder were also shifted to lower 2θ values compared to the peaks of pure Ni oxalate powder, which indicated expansion of the crystal lattice.[106] The lattice parameters calculated for the blend oxalate dihydrate were $a = 11.99$ Å, $b = 5.53$ Å, and $c = 15.62$ Å, compared with those of $NiC_2O_4 \cdot 2H_2O$ being $a = 11.75$ Å, $b = 5.28$ Å, and $c = 15.52$ Å.[107] The shift in the lattice parameters with the addition of Mn to the precipitation solution indicated incorporation of larger size Mn ions ($Mn^{2+} = 0.81$ Å, $Ni^{2+} = 0.69$ Å) into the crystal, consistent with homogeneous precipitation of the TM oxalates and not independent precipitation of individual $MnC_2O_4 \cdot 2H_2O$ and $NiC_2O_4 \cdot 2H_2O$ particles.

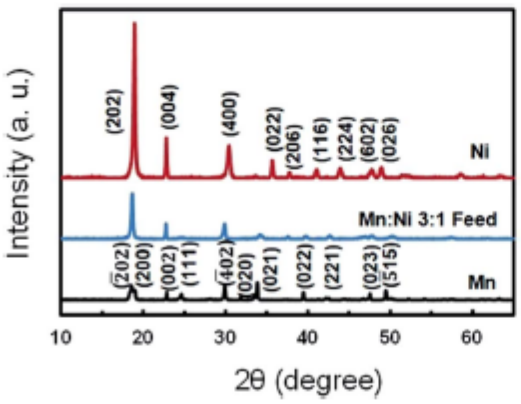

Fig. 4 XRD patterns of $NiC_2O_4 \cdot 2H_2O$ (red), Mn : Ni 3 : 1 feed oxalate dihydrate (blue), and $MnC_2O_4 \cdot 2H_2O$ (black). Miller indices correspond to orthorhombic and monoclinic symmetries for $NiC_2O_4 \cdot 2H_2O$ and $MnC_2O_4 \cdot 2H_2O$, respectively.

Previous studies have also shown Mn–Ni forms a solid solution when precipitated with oxalate.[102,106,108] Unexpectedly, even though the blend system has 75% Mn and $MnC_2O_4 \cdot 2H_2O$ precipitates faster than $NiC_2O_4 \cdot 2H_2O$, the resulting phase was consistent with the β-$NiC_2O_4 \cdot 2H_2O$ instead of α-$MnC_2O_4 \cdot 2H_2O$. Thus, the β-$NiC_2O_4 \cdot 2H_2O$ phase was favourable at these solution conditions. Whether the blend oxalate is α- or β-oxalate is dependent on the synthesis conditions.[92] We are currently exploring the detailed phase diagram for these oxalate materials and this topic will be the subject of a future publication; however, it appears that under the majority of solution compositions in the Mn–Ni blend system, adjusting only the Mn : Ni ratio, the β-$NiC_2O_4 \cdot 2H_2O$ was the preferred structure. The extent of Mn precipitation was greater in the blend system compared to pure $MnC_2O_4 \cdot 2H_2O$ (Fig. 2). This observation also suggested that the β-$NiC_2O_4 \cdot 2H_2O$ structure facilitated a greater extent of Mn precipitation relative to the α phase crystal structure that forms in the pure Mn precipitation.

TGA analyses were conducted on the three oxalate samples. The dehydration step, which occurs below 200 °C, caused a mass loss of ~20% for all samples, which indicated the oxalate precursors synthesized were dihydrates (Mn and Ni composition of $Mn_{0.72}Ni_{0.28}C_2O_4 \cdot 2H_2O$ for the blend precursors from ICP, feed was 3 : 1 Mn : Ni). Both the dehydration temperature and the oxalate decomposition temperature are greater for $NiC_2O_4 \cdot 2H_2O$ than for $MnC_2O_4 \cdot 2H_2O$, indicating that the thermal stability of $NiC_2O_4 \cdot 2H_2O$ was greater. In the case of $Mn_{0.72}Ni_{0.28}C_2O_4 \cdot 2H_2O$, the dehydration and oxalate decomposition peaks were between the values for $NiC_2O_4 \cdot 2H_2O$ and $MnC_2O_4 \cdot 2H_2O$. The relatively broad and high temperature for the dehydration peak, however, suggested the structural water was in an environment more similar to that of $NiC_2O_4 \cdot 2H_2O$. This observation was consistent with the XRD patterns indicating that the blend oxalate structure was consistent with $NiC_2O_4 \cdot 2H_2O$. TGA profiles and full discussions can be found in the ESI, Fig. S2.†

Synthesis of slight variations of Mn : Ni ratio stoichiometry materials

As discussed above, solution equilibrium calculations provide insights into selecting feed stoichiometry, but these calculations alone were not quantitative enough to use for predictive

synthesis, particularly at low solution concentrations desirable for tuneable particle morphologies. Quantitative predictive models incorporating the precipitation rate will be a long-term goal; however, further study and information on particle size distribution as a function of time will be needed to appropriately normalize the precipitation rate. To further demonstrate the importance of working towards these predictive synthesis methods, two additional blend oxalate precipitates were synthesized such that three resulting precursors were made: one that was almost exactly at the desired 3 : 1 Mn : Ni stoichiometry, one that was enriched in Ni (<3 : 1), and one that was enriched in Mn (>3 : 1). All oxalates were synthesized using 20 mM total TM and the particles were collected after 30 minutes to be consistent with earlier procedures. The 3 : 1 Mn : Ni feed from the earlier experiments resulted in 2.6 : 1 Mn : Ni, confirmed using ICP on digested powders, and this served as the Ni-rich sample. A feed ratio of 3.52 : 1 resulted in 3.02 : 1 Mn : Ni (the stoichiometric sample), and 3.82 : 1 feed resulted in 3.33 : 1 Mn : Ni (Mn-rich sample). The compositional deviation between equilibrium calculations and measurements varied from ~5–15%. After calcination of the oxalate samples in the presence of lithium, the detailed compositions of the three "LMNO" materials were $LiMn_{1.46}Ni_{0.54}O_4$, $LiMn_{1.50}Ni_{0.50}O_4$, and $LiMn_{1.54}Ni_{0.46}O_4$ which will be referred to as Ni-rich, stoichiometric, and Mn-rich LMNO, respectively. These listed compositions have Mn : Ni ratios consistent with ICP measurements on the final active material and assume a Li : TM ratio of 1 : 2 and TM : O ratio of 1 : 2. Actual Li : TM ratios and a summary of compositional information determined by ICP can be found in ESI, Table S2.†

Characterization of the stoichiometric and non-stoichiometric LMNO materials

The three LMNO samples were synthesized to demonstrate that small compositional variations during coprecipitation synthesis, when not accounting for the deviation from feed stoichiometry, can result in detectable changes to the final active material after calcination. LMNO is cubic with Li on the tetrahedral sites of the structure. Depending on the distribution of Mn and Ni ions in the lattice, LMNO has two different crystallographic structures: with disordered Ni and Mn on the octahedral sites the cubic spinel has the space group $Fd\bar{3}m$, while with higher ordering of Ni^{2+} and Mn^{4+} it has the space group $P4_332$. In synthesizing spinel LMNO the high calcination temperature leads to the reduction of manganese from Mn^{4+} to Mn^{3+}, which results in the $Fd\bar{3}m$ disordered structure.[109] Annealing at 700 °C for extended periods has been reported to reoxidize the Mn^{3+} back to Mn^{4+} and may convert the spinel to the primitive cubic ordered structure.[34,110]

Achieving the appropriate chemical composition is essential for extracting the maximum capacity from LMNO materials. For the molecular ratio of Mn : Ni 3 : 1, theoretically all the electrochemical capacity comes from the Ni^{2+}/Ni^{4+} redox couple. When there is Mn : Ni deviation from 3 : 1; however, either Mn-rich or Ni-rich materials may result in changes to the oxidation state and/or the crystal phase, thus influencing the electrochemical performance. Since Ni in $LiNi_{0.5}Mn_{1.5}O_4$ is Ni^{2+}, we assume that nickel ions in the whole series of Mn-rich $LiNi_xMn_{2-x}O_4$ materials with $0 < x < 0.5$ are also Ni^{2+}. Taking charge neutrality into account, the Mn^{3+} and Mn^{4+} content in the materials can be written as $LiNi_x^{2+}Mn_{1-2x}^{3+}Mn_{1+x}^{4+}O_4$. Assuming that the 4.7 V high voltage capacity comes from the Ni redox, and that Mn^{3+}/Mn^{4+} redox gives a ~4.1 V plateau during cycling, we expect to get $2x$ Li capacity per formula unit at ~4.7 V and $(1 - 2x)$ Li capacity at ~4.1 V, which have been observed experimentally.[6,74,79,111–113] Within the Mn-rich range, the material should be stable in the spinel phase, $LiMn_2O_4$ being the extreme case, though more Mn content results in a higher fraction of Mn^{3+} ions which potentially results in Jahn–Teller distortion, being detrimental to the structural stability. For Ni-rich materials ($0.5 < x < 1$), we assume the Mn^{4+} will not be further oxidized, and thus the oxidation state of Ni ions will be increased from Ni^{2+} to Ni^{3+} to meet charge neutrality and the result would be $LiNi_{1-x}^{2+}Ni_{2x-1}^{3+}Mn_{2-x}^{4+}O_4$. Summing up the Ni^{2+}/Ni^{4+} and the Ni^{3+}/Ni^{4+} couples, the high voltage capacity would be constant through the compositional range, $LiNi^{3+}Mn^{4+}O_4$ being the extreme case. Based on the analysis above, if the compositional deviation was Ni-rich, a reduction in the high voltage electrochemical capacity would not be expected. However, as the Ni content increases, the risk of forming a rock-salt impurity phase significantly increases, which potentially deteriorates both the electronic conductivity, ionic conductivity, and total active material and thus energy density. The end point material, $LiNi^{3+}Mn^{4+}O_4$ was previously reported to have a rock-salt structure, showing XRD patterns consistent with $LiNiO_2$.[72,74,109] This means that there are likely multiple phases coexisting across some range of compositions in the Ni-rich regime. The formation of layered structures also presents the risk of phase segregation in the material, because Li–Mn–O has limited stability as a layered structure.[6,74,79,111,112] SEM images of the three precursors and their corresponding final oxide samples can be found in ESI, Fig. S3.† All the precursors exhibit hexagonal platelet secondary particle morphologies and similar secondary particle sizes of about 20 μm. The secondary particles were comprised of multi-faceted primary particles with length scales of approximately a couple hundred nanometers. The overall morphologies of the LMNO samples exhibit no significant differences and were not expected to contribute significantly to any observed differences in electrochemical cell performance.

XRD patterns for Ni-rich, stoichiometric, and Mn-rich LMNO powders are shown in Fig. 5. The peaks, except those marked with an *, all can be indexed to $Fd\bar{3}m$ spinel cubic structures. The Ni-rich sample contains impurity peaks, and their location was consistent with previous reports of $Li_xNi_{1-x}O_2$ structures.[72,74,109] This implies that the higher fraction of nickel cannot be accommodated in the LMNO structure and thus the Ni enrichment facilitates the formation of the rock-salt impurity. The impurity phase was not observed in the Mn-rich LMNO sample.

Rietveld refinements were done using only the $Fd\bar{3}m$ space group and the resulting lattice parameters of the three LMNO samples were 8.2046 Å, 8.1909 Å, and 8.1934 Å for Ni-rich, stoichiometric, and Mn-rich samples, respectively. The larger lattice parameter for the Ni-rich LMNO sample was attributed to

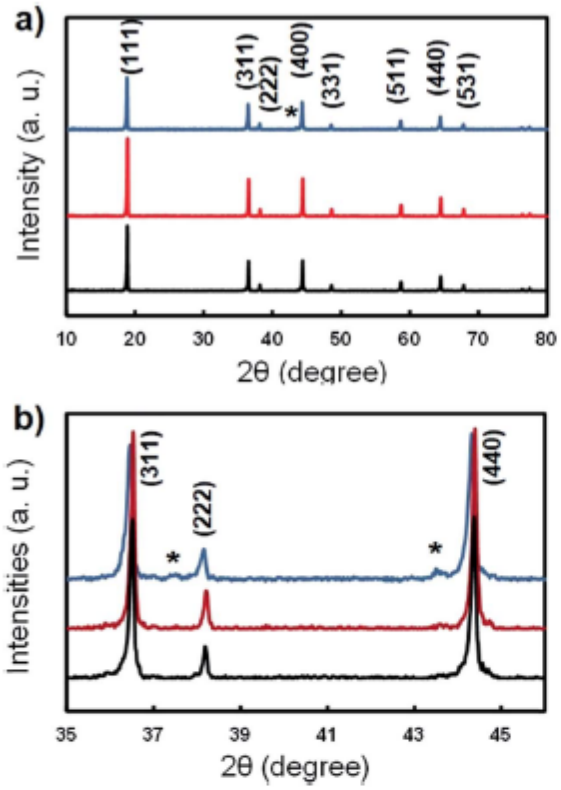

Fig. 5 (a) XRD patterns of Ni-rich (blue), stoichiometric (red), and Mn-rich (black) LMNO. (b) Close up of patterns in (a) between 35–46 degrees to better highlight the rock-salt impurity phase peaks (marked with *).

the higher Ni ion content, since the ionic radius of Ni^{3+} (0.70 Å) is larger than the average of Mn^{4+} (0.53 Å) and Ni^{2+} (0.69 Å).[30] Though some of the Ni distributes into the impurity phase, the high Ni content likely helps to ensure high Ni within the LMNO structure as well. The slightly higher lattice parameter of the Mn-rich LMNO sample relative to the stoichiometric sample may have been due to the relatively increased amount of Mn^{3+} (0.645 Å), whose ionic radius is greater than the average of Mn^{4+} (0.53 Å) and Ni^{2+} (0.69 Å). Relative peak intensities reflect the relative exposure degree of surface orientations in the spinel structure.[74,114,115] By normalizing to the (311) peak of the three patterns, the relative intensities were compared of the high-active[111] crystal facet, which were 2.066, 2.100, and 2.186 for Ni-rich, stoichiometric, and Mn-rich LMNO samples respectively. The similar values implied that the exposure degrees of the high-active[111] facet was not expected to contribute to differences in electrochemical measurements.

The discharge curves of Li/LMNO coin cells, all charged/discharged at a rate of C/10, are shown in Fig. 6. The stoichiometric LMNO had the highest first cycle discharge capacity of 123 mA h g^{-1}, while the Mn-rich and Ni-rich LMNO show similar capacities of around 115 mA h g^{-1}. The discharge capacity was divided into the high (4.9 to 4.1 V, *vs.* Li/Li^+) and low (4.1 to 3.6 V, *vs.* Li/Li^+) voltage ranges for comparison,

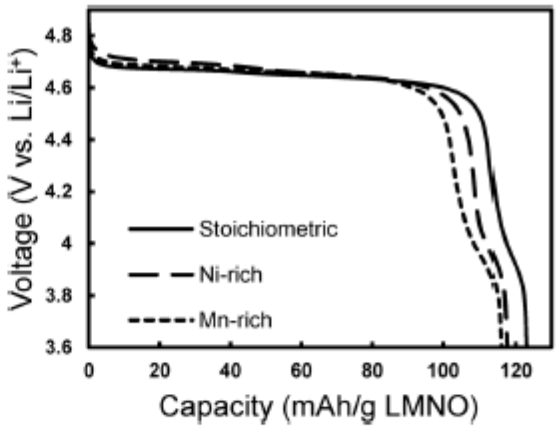

Fig. 6 Discharge profiles of stoichiometric, Ni-rich, and Mn-rich Li/LMNO cells cycled at a rate of C/10 (147 mA g^{-1} LMNO).

corresponding to primarily Ni^{2+}/Ni^{4+} and Mn^{3+}/Mn^{4+} redox couples, respectively. Table 1 lists the electrochemical capacities of the three LMNO materials within these potential ranges, and also the calculated Mn^{3+} and Ni^{2+} amounts based on these capacities. All the discharge capacities in Table 1 were averages of results from three different cells for each representative LMNO sample. The low voltage capacities of the Ni-rich LMNO and stoichiometric LMNO were nearly identical, and thus so were the calculated amounts of Mn^{3+}. The Mn^{3+} formation occurs to some extent during the high temperature calcination procedure, regardless of the composition of the samples. The Mn-rich LMNO, however, had a greater capacity within the low voltage range, which was attributed to higher amounts of Mn^{3+} in the structure. The higher fraction of Mn^{3+} observed was also consistent with the larger lattice parameters and the expected composition of $LiNi_{0.46}{}^{2+}Mn_{0.08}{}^{3+}Mn_{1.46}{}^{4+}O_4$ with 0.08 mol Mn^{3+} per formula, which was close to 0.09 mol Mn^{3+} per mole of LMNO calculated based on the low voltage range capacity. In comparing Mn-rich LMNO and stoichiometric LMNO, the amount of Ni^{2+} in the materials was calculated by assuming that all the high voltage capacity came from the $Ni^{2+}/Ni^{3+}/Ni^{4+}$ redox couple(s) (Table 1). Even in the stoichiometric sample, the Ni redox couple cannot be fully exploited during charge or discharge, possibly due to ion diffusion or electron exchange limitations.[25,63,116] The Ni^{2+} amount calculated from the electrochemical capacities of the Mn-rich material contains 94% the Ni^{2+} of the stoichiometric sample, close to the theoretical Ni^{2+} percentage of 92% obtained by comparing $LiNi_{0.46}{}^{2+}Mn_{0.08}{}^{3+}Mn_{1.46}{}^{4+}O_4$ to $LiNi_{0.5}Mn_{1.5}O_4$. This implies that the intrinsic capacity losses relative to the theoretical capacity appears to be proportionally lost by Ni^{2+} in the materials. Therefore, the detailed chemical composition of LMNO samples provides insights into the expected relative capacities in the low voltage and high voltage regions of the material, in particular when comparing Mn-rich and stoichiometric LMNO materials. This analysis was consistent with previous reports in the literature and was consistent with analysis of the dQ/dV plots of the electrode materials (see Fig. S4 in ESI† for the dQ/dV plots and

Table 1 Summaries of the Ni-rich, stoichiometric, and Mn-rich LMNO discharge capacities. Standard deviations for capacity values were based on 5 discharge cycles of 3 cells for each material

		Specific capacity (mA h g^{-1})			TM ion amount per mole of LMNO based on capacities	
Sample	Mn : Ni (ICP)	Total	Low voltage	High voltage	Mn^{3+} (mol)	Ni^{2+a} (mol)
Nickel-rich	1.46 : 0.54	118.6 ± 5.0	9.9 ± 1.3	108.7 ± 3.7	0.07	0.37
Stoichiometric	1.50 : 0.50	121.8 ± 2.4	9.5 ± 1.0	112.3 ± 3.0	0.06	0.38
Manganese-rich	1.54 : 0.46	118.2 ± 1.9	12.6 ± 1.0	105.5 ± 1.0	0.09	0.36

[a] The Ni^{2+} amount was calculated assuming all the high voltage capacity was from Ni^{2+}/Ni^{4+} redox couple.

further discussion).[78,109,113] Detailed comparison between Ni-rich and stoichiometric LMNO was not quite as straightforward because the impurity phase in the Ni-rich sample complicates the analysis. The quantity of the impurity phase for the Ni-rich LMNO appears to have been insufficient to significantly reduce the material capacity, though capacity decreases caused by more substantial proportions of the rock-salt impurity for Ni-rich LMNO samples have been previously established in the literature.[74] Similar levels of exposure of the high-active facet, as aforementioned, and similar Mn^{3+} in the stoichiometric and Ni-rich materials (Table 1) likely made identification of the electrochemical performance differences due to the compositional variation more difficult to observe.

Cycle life testing of Li/LMNO coin cells was also conducted and the results can be found in ESI Fig. S5.† All cells had similar capacity fade after 200 charge/discharge cycles at C/10. The specific discharge capacities after 200 cycles were 112.9 mA h g^{-1}, 115.9 mA h g^{-1}, and 107.1 mA h g^{-1} with capacity retentions of 95.2%, 97.4%, and 91.9% (relative to the 10^{th} cycle) for the stoichiometric, Ni-rich, and Mn-rich LMNO materials, respectively. All cells appeared to have an activation-related capacity increase for the first several cycles, thus the 10^{th} cycle was chosen for relative capacity retention.[63,73,117,118] While the stoichiometric LMNO had encouraging results both with regards to total capacity and capacity retention, the relatively small differences between the three materials makes it premature to assign achieving the stoichiometric composition as improving these two metrics without more extensive cell testing and analysis. Interestingly, the first cycle coulombic efficiency (CE) was significantly different for the three materials, where the values were 90.8%, 85.9%, and 88.7% for stoichiometric, Ni-rich, and Mn-rich LMNO, respectively. The CE of the first few cycles is an indicator of the stability of the electrode–electrolyte interface and high CE indicates a stable interface.[74] The high CE of the stoichiometric LMNO suggested it formed a relatively stable electrode–electrolyte interface, though more detailed investigations would be needed to confirm the stoichiometry at the interface of these materials with differing bulk compositions and the potential impact on the resulting solid-electrolyte interphase.

Conclusions

Coprecipitation is a popular route to synthesize Li-ion battery precursors, and performing coprecipitation in low solution concentration regimes can enable explicit tuning of morphology of battery precursor materials. A study was conducted to determine how significant the deviation in composition of multicomponent TM precursors may be from feed stoichiometries in a low concentration condition, using a model system containing Mn^{2+}, Ni^{2+}, and $C_2O_4^{2-}$ as coprecipitation species. Equilibrium calculations suggest deviation between feed and resulting precursor stoichiometry, which had qualitative but not quantitative agreement. Experiments tracking the extent of precipitation of each of the TM species suggests that while TMs have very different rates in isolation, the faster precipitating species results in seed particles that result in nearly 1 : 1 precipitation of Ni and Mn when precipitated from the same solution. Synthesis of precursor particles that were produced using 3 : 1 Mn : Ni feed (Ni-enriched precipitate), 3 : 1 Mn : Ni precipitate, and an intentionally Mn-enriched precipitate demonstrated that even small deviations in relative Mn : Ni stoichiometry can have detectable impacts on material structure and electrochemical properties – though for these relatively small compositional deviations the material properties were not extreme. These results suggested that careful consideration of solution chemistry, including equilibrium distribution of TM and the rate at which different TM are precipitated, should be given more careful consideration during the synthesis of battery materials using coprecipitation methods. While in this study low concentrations of TM were used which was more relevant to morphology tuning of active materials important for investigating morphology effects on electrochemical properties, these results are also extendable to some effects observed with more concentrated solutions. In particular, the incorporation of chelating agents commonly used in larger scale coprecipitation will intensify compositional deviations between feed stoichiometry and particle stoichiometry even at relatively high TM concentrations.

Experimental methods

Preparation of oxalate precursor and cathode active material particles

Laboratory grade $MnSO_4 \cdot H_2O$, $NiSO_4 \cdot 6H_2O$, and $Na_2C_2O_4$ (all from Fisher) were used for the coprecipitation synthesis. TM sulfate and oxalate reagents were dissolved separately in deionized (DI) water to prepare TM solution and oxalate solution, and both solutions were heated to 60 °C. The TM solution

was then poured all at once into the oxalate solution to start the coprecipitation reaction. The total volumes of the mixed solutions were 0.8 L (within a 1 L beaker) for all syntheses, and the reagent masses were adjusted to each desired solution concentration and TM feed ratio. The temperature was maintained during the reaction at 60 °C using a hot plate. The coprecipitation solution was stirred continuously at 300 rpm with a magnetic stirrer to keep the solution homogeneous during the precipitate formation and to prevent particles from settling within the suspension. The particles were collected by vacuum filtration after 30 minutes, and then rinsed with ~2 L DI water before drying in the oven (carbolite) at 80 °C overnight. The precursor particles were mixed with 5% excess LiOH with 1 : 2 Li : TM ratio using a mortar and pestle by hand for 5 minutes. This mixture was then fired in the furnace (carbolite CWF 1300 box furnace) in an air atmosphere at 850 °C for 6 hours to obtain the final active material (with the target composition generally being $LiMn_{1.5}Ni_{0.5}O_4$). The furnace temperature ramp rate was set at 1 °C per minute, and during the firing process the temperature was programmed for holds at 200 °C and 350 °C each for 2 hours to complete the individual steps of the structural water loss and oxalate decomposition, respectively.

Solution equilibrium calculations

Equilibrium calculations were performed using OLI™ Studio 9.2. Calculations were also performed using an appropriate system of equations including solubility constants and complexation constants[119] combined with an appropriate numerical optimization package.[71] We noted that the equilibrium concentrations of the various solution species did not deviate significantly when using literature data and numerical optimization compared to commercial OLI™ calculations; however, the OLI™ values are the only ones reported in this study because they incorporated temperature influences, and this information was not readily available in the literature.

Rate of precipitation of Ni and Mn

Experiments were conducted to determine the concentration of each soluble TM remaining in the solution as a function of coprecipitation time. The reactor vessels were 1 L beakers and solutions were prepared in the same manner as described above. At periodic time intervals during the coprecipitation, a sample (~2 mL) was withdrawn from the 1 L beaker using a 3 mL syringe. For the withdrawn sample, the aqueous phase was quickly separated from the solid precipitate particles by forcing the solution through a 33 mm diameter syringe filter with 0.22 μm pore size (Fisherbrand). The aqueous phase was further digested using aqua regia and diluted with DI water into a proper concentration for inductively coupled plasma optical emission spectroscopy (ICP) analysis (PerkinElmer Optima 8000). The typical concentration range for ICP analysis was 0.1 to 100 ppm for Mn and Ni. Samples were continuously collected along the course of the reaction and the TM concentrations remaining in the aqueous phase were obtained as a function of reaction time. The total volume collected during the experiment for compositional analysis was typically 30 mL, or 3.5% of the total initial solution volume.

Material characterization and electrochemical evaluation

The chemical compositions of the precursors were measured using ICP analysis after the powders were digested with aqua regia and diluted to appropriate concentrations for analysis. The morphologies of the oxalate precursor and calcined final active materials were characterized with a scanning electron microscope (SEM, FEI Quanta 650). The crystal structure of the materials were analyzed by powder X-ray diffraction (XRD) with a PANalytical X'pert ProMPD using a Cu-Kα radiation source. Thermal gravimetrical analysis (TGA, TA Q50) was conducted to confirm the amount of the structural water and the weight loss profile of the oxalate precursors. All thermal measurements were performed in air at a heating rate of 10 °C min^{-1}. Electrochemical testing was performed using CR2032-type coin cells. The cathodes were fabricated by blending 80 wt% active material, 10 wt% acetylene black as the conductive additive, and 10 wt% polyvinylidene difluoride binder (dissolved in *N*-methyl-2-pyrrolidone as the solvent) first by hand with mortar and pestle and then in a slurry mixer (Thinky) for 6 minutes. The mixed electrode slurry was then pasted onto an aluminum foil current collector with an AFA-3 automatic film coater (MTI) and using a doctor blade with a gap thickness of 200 μm. The electrode was dried at 80 °C overnight in an oven in air, followed by another 3 hour vacuum drying at 80 °C prior to punching into 14 mm diameter electrode disks. The loading of active material in electrodes evaluated were all between 7.2 and 12.8 mg (4.5 and 8.0 mg cm^{-2}). Coin cells were assembled inside an argon-filled glove box (<1 ppm O_2 and H_2O) with a single thin film of lithium metal as the counter and reference anode. Cel-gard 2325 trilayer membrane was used as the separator. The electrolyte was 1.2 M $LiPF_6$ dissolved in ethylene carbonate (EC) and ethyl methyl carbonate (EMC) (3 : 7 vol%). The cells were tested in the voltage range of 3.6–4.9 V at room temperature using a MACCOR multichannel battery cycler. Where C rates are given, 1C was assumed to correspond to 14.7 mA g^{-1} LMNO active material.

Acknowledgements

The authors acknowledge financial support from the National Science Foundation through awards CBET-1652488 and ECCS-1405134. The authors also thank Prof. Geoff Geise for use of their lab's TGA instrument.

Notes and references

1 M. Armand and J.-M. Tarascon, Building better batteries, *Nature*, 2008, **451**(7179), 652–657, DOI: 10.1038/451652a.
2 E. Lee, K.-W. Nam, E. Hu and A. Manthiram, Influence of Cation Ordering and Lattice Distortion on the Charge–Discharge Behavior of $LiMn_{1.5}Ni_{0.5}O_4$ Spinel between 5.0 and 2.0 V, *Chem. Mater.*, 2012, **24**, 3610–3620.
3 M. Casas-Cabanas, C. Kim, J. Rodriguez-Carvajal and J. Cabana, Atomic scale drivers of ordering transitions in

$LiNi_{0.5}Mn_{1.5}O_4$ and relationship with electrochemical properties, *J. Mater. Chem. A*, 2016, 8255–8262.

4 T. Kozawa, T. Murakami and M. Naito, Insertion of lattice strains into ordered $LiNi_{0.5}Mn_{1.5}O_4$ spinel by mechanical stress: a comparison of perfect *versus* imperfect structures as a cathode for Li-ion batteries, *J. Power Sources*, 2016, **320**, 120–126, DOI: 10.1016/j.jpowsour.2016.04.086.

5 K. Saravanan, A. Jarry, R. Kostecki and G. Chen, A study of room-temperature $Li_xMn_{1.5}Ni_{0.5}O_4$ solid solutions, *Sci. Rep.*, 2015, **5**(111), 8027.

6 H. Duncan, B. Hai, M. Leskes, C. P. Grey and G. Chen, Relationships between Mn^{3+} Content, Structural Ordering, Phase Transformation, and Kinetic Properties in $LiNi_xMn_{2-x}O_4$ Cathode Materials, *Chem. Mater.*, 2014, **26**(18), 5374–5382, DOI: 10.1021/cm502607v.

7 S. Patoux, L. Daniel, C. Bourbon, H. Lignier, C. Pagano, F. Le Cras, *et al.*, High voltage spinel oxides for Li-ion batteries: From the material research to the application, *J. Power Sources*, 2009, **189**(1), 344–352.

8 M. M. Thackeray, C. S. Johnson, J. T. Vaughey, N. Li and S. A. Hackney, Advances in manganese-oxide "composite" electrodes for lithium-ion batteries, *J. Mater. Chem.*, 2005, **15**(23), 2257–2267, DOI: 10.1039/b417616m.

9 S.-H. Kang, P. Kempgens, S. Greenbaum, A. J. Kropf, K. Amine and M. M. Thackeray, Interpreting the structural and electrochemical complexity of $0.5Li_2MnO_3$–$0.5LiMO_2$ electrodes for lithium batteries ($M = Mn_{0.5-x}Ni_{0.5-x}Co_{2x}$, $0 \leq x \leq 0.5$), *J. Mater. Chem.*, 2007, **17**(20), 2069–2077, DOI: 10.1039/b618715c.

10 S.-H. Kang, C. S. Johnson, J. T. Vaughey, K. Amine and M. M. Thackeray, The Effects of Acid Treatment on the Electrochemical Properties of $0.5Li_2MnO_3 \cdot 0.5LiNi_{0.44}Co_{0.25}Mn_{0.31}O_2$ Electrodes in Lithium Cells, *J. Electrochem. Soc.*, 2006, **153**(6), A1186–A1192.

11 J.-S. Kim, C. S. Johnson and M. M. Thackeray, Layered $xLiMO_2 \cdot (1-x)\ Li_2M'O_3$ electrodes for lithium batteries: a study of $0.95LiMn_{0.5}Ni_{0.5}O_2 \cdot 0.05Li_2TiO_3$, *Electrochem. Commun.*, 2002, **4**(3), 205–209.

12 D. Kim, S.-H. H. Kang, M. Balasubramanian and C. S. Johnson, High-energy and high-power Li-rich nickel manganese oxide electrode materials, *Electrochem. Commun.*, 2010, **12**(11), 1618–1621, DOI: 10.1016/j.elecom.2010.09.009.

13 J. Zheng, M. Gu, J. Xiao, B. J. Polzin, P. Yan, X. Chen, *et al.*, Functioning Mechanism of AlF_3 Coating on the Li- and Mn-Rich Cathode Materials, *Chem. Mater.*, 2014, **26**(22), 6320–6327, DOI: 10.1021/cm502071h.

14 S. Hwang, S. M. Kim, S.-M. Bak, S. Y. Kim, B.-W. Cho, K. Y. Chung, *et al.*, Using Real-Time Electron Microscopy To Explore the Effects of Transition-Metal Composition on the Local Thermal Stability in Charged $Li_xNi_yMn_zCo_{1-y-z}O_2$ Cathode Materials, *Chem. Mater.*, 2015, **27**(11), 3927–3935, DOI: 10.1021/acs.chemmater.5b00709.

15 F. Yang, Y. Liu, S. K. Martha, Z. Wu, J. C. Andrews, G. E. Ice, *et al.*, Nanoscale Morphological and Chemical Changes of High Voltage Lithium–Manganese Rich NMC Composite Cathodes with Cycling, *Nano Lett.*, 2014, **14**(8), 4334–4341, DOI: 10.1021/nl502090z.

16 J. Li, R. Klöpsch, M. C. Stan, S. Nowak, M. Kunze, M. Winter, *et al.*, Synthesis and electrochemical performance of the high voltage cathode material $Li[Li_{0.2}Mn_{0.56}Ni_{0.16}Co_{0.08}]O_2$ with improved rate capability, *J. Power Sources*, 2011, **196**(10), 4821–4825.

17 D. Mohanty, S. Kalnaus, R. A. Meisner, K. J. Rhodes, J. Li, E. A. Payzant, *et al.*, Structural transformation of a lithium-rich $Li_{1.2}Co_{0.1}Mn_{0.55}Ni_{0.15}O_2$ cathode during high voltage cycling resolved by *in situ* X-ray diffraction, *J. Power Sources*, 2013, **229**, 239–248.

18 I. Lee, J. Kim, S. Han, J.-I. Park, J.-M. Lee, D.-H. Kim, *et al.*, Communication—Preparation of Highly Monodisperse Ni-Rich Cathode Material for Lithium Ion Batteries, *J. Electrochem. Soc.*, 2016, **163**(7), A1336–A1339.

19 R. Robert, C. Bünzli, E. J. Berg and P. Novák, Activation Mechanism of $LiNi_{0.80}Co_{0.15}Al_{0.05}O_2$: Surface and Bulk Operando Electrochemical, Differential Electrochemical Mass Spectrometry, and X-ray Diffraction Analyses, *Chem. Mater.*, 2015, **27**(2), 526–536, DOI: 10.1021/cm503833b.

20 N. Wu, H. Wu, H. Liu and Y. Zhang, Solvothermal coating $LiNi_{0.8}Co_{0.15}Al_{0.05}O_2$ microspheres with nanoscale Li_2TiO_3 shell for long lifespan Li-ion battery cathode materials, *J. Alloys Compd.*, 2016, **665**, 48–56.

21 S. Hwang, W. Chang, S. M. Kim, D. Su, D. H. Kim, J. Y. Lee, *et al.*, Investigation of Changes in the Surface Structure of $Li_xNi_{0.8}Co_{0.15}Al_{0.05}O_2$ Cathode Materials Induced by the Initial Charge, *Chem. Mater.*, 2014, **26**(2), 1084–1092, DOI: 10.1021/cm403332s.

22 F. Dogan, J. T. Vaughey, H. Iddir and B. Key, Direct Observation of Lattice Aluminum Environments in Li Ion Cathodes $LiNi_{1-y-z}Co_yAl_zO_2$ and Al-Doped $LiNi_xMn_yCo_zO_2$ *via* ^{27}Al MAS NMR Spectroscopy, *ACS Appl. Mater. Interfaces*, 2016, **8**(26), 16708–16717, DOI: 10.1021/acsami.6b04516.

23 G. Liu, K.-S. Park, J. Song and J. B. Goodenough, Influence of thermal history on the electrochemical properties of Li $[Ni_{0.5}Mn_{1.5}]O_4$, *J. Power Sources*, 2013, **243**, 260–266.

24 M. Hu, X. Pang and Z. Zhou, Recent progress in high-voltage lithium ion batteries, *J. Power Sources*, 2013, **237**, 229–242, DOI: 10.1016/j.jpowsour.2013.03.024.

25 M. Kunduraci and G. G. Amatucci, The effect of particle size and morphology on the rate capability of 4.7 V $LiMn_{1.5} + \delta Ni_{0.5} - \delta O_4$ spinel lithium-ion battery cathodes, *Electrochim. Acta*, 2008, **53**(12), 4193–4199.

26 J. B. Goodenough and K.-S. S. Park, The Li-Ion Rechargeable Battery: A Perspective, *J. Am. Chem. Soc.*, 2013, **135**(4), 1167–1176, DOI: 10.1021/ja3091438.

27 J. B. Goodenough and Y. Kim, Challenges for rechargeable Li batteries, *Chem. Mater.*, 2010, **22**(3), 587–603.

28 T. F. Yi, J. Mei and Y. R. Zhu, Key strategies for enhancing the cycling stability and rate capacity of $LiNi_{0.5}Mn_{1.5}O_4$ as high-voltage cathode materials for high power lithium-ion batteries, *J. Power Sources*, 2016, **316**, 85–105, DOI: 10.1016/j.jpowsour.2016.03.070.

29 N. R. Van, The rechargeable revolution: A better battery, *Nature*, 2014, **507**, 26–28.
30 C. M. Julien and A. Mauger, Review of 5 V electrodes for Li-ion batteries: Status and trends, *Ionics*, 2013, **19**(7), 951–988.
31 D. Liu, J. Han and J. B. Goodenough, Structure, morphology, and cathode performance of $Li_{1-x}[Ni_{0.5}Mn_{1.5}]O_4$ prepared by coprecipitation with oxalic acid, *J. Power Sources*, 2010, **195**(9), 2918–2923.
32 A. Van Der Ven, J. Bhattacharya and A. Belak, Understanding Li Diffusion in Li-Intercalation Compounds, *Acc. Chem. Res.*, 2013, **46**(5), 1216–1225.
33 D. Liu, W. Zhu, J. Trottier, C. Gagnon, F. Barray, A. Guerfi, *et al.*, Spinel materials for high-voltage cathodes in Li-ion batteries, *RSC Adv.*, 2014, **4**(1), 154–167.
34 L. Wang, H. Li, X. Huang and E. Baudrin, A comparative study of $Fd\bar{3}m$ and $P4332$ "$LiNi_{0.5}Mn_{1.5}O_4$", *Solid State Ionics*, 2011, **193**(1), 32–38.
35 K. R. Chemelewski, E. S. Lee, W. Li and A. Manthiram, Factors influencing the electrochemical properties of high-voltage spinel cathodes: relative impact of morphology and cation ordering, *Chem. Mater.*, 2013, **25**(14), 2890–2897.
36 B. L. Cushing and J. B. Goodenough, Influence of carbon coating on the performance of a $LiMn_{0.5}Ni_{0.5}O_2$ cathode, *Solid State Sci.*, 2002, **4**(11), 1487–1493.
37 X.-Q. Yang, J. McBreen, W.-S. Yoon and C. P. Grey, Crystal structure changes of $LiMn_{0.5}Ni_{0.5}O_2$ cathode materials during charge and discharge studied by synchrotron based *in situ* XRD, *Electrochem. Commun.*, 2002, **4**(8), 649–654.
38 W.-S. Yoon, C. P. Grey, M. Balasubramanian, X.-Q. Yang and J. McBreen, *In situ* X-ray Absorption Spectroscopic Study on $LiNi_{0.5}Mn_{0.5}O_2$ Cathode Material during Electrochemical Cycling, *Chem. Mater.*, 2003, **15**(16), 3161–3169, DOI: 10.1021/cm030220m.
39 F. Amalraj, D. Kovacheva, M. Talianker, L. Zeiri, J. Grinblat, N. Leifer, *et al.*, Synthesis of Integrated Cathode Materials xLi_2MnO_3 $(1-x)LiMn_{1/3}Ni_{1/3}Co_{1/3}O_2$ $(x = 0.3, 0.5, 0.7)$ and Studies of Their Electrochemical Behavior, *J. Electrochem. Soc.*, 2010, **157**(10), A1121–A1130.
40 C. S. Johnson, N. Li, C. Lefief, J. T. Vaughey and M. M. Thackeray, Synthesis, Characterization and Electrochemistry of Lithium Battery Electrodes: $xLi_2MnO_3 \cdot (1-x)LiMn_{0.333}Ni_{0.333}Co_{0.333}O_2$ $(0 \leq x \leq 0.7)$, *Chem. Mater.*, 2008, **20**(19), 6095–6106, DOI: 10.1021/cm801245r.
41 P. Lanz, C. Villevieille and P. Novák, *Ex situ* and *in situ* Raman microscopic investigation of the differences between stoichiometric $LiMO_2$ and high-energy $xLi_2MnO_3 \cdot (1-x)LiMO_2$ (M = Ni, Co, Mn), *Electrochim. Acta*, 2014, **130**, 206–212.
42 M. M. Thackeray, S.-H. Kang, C. S. Johnson, J. T. Vaughey, R. Benedek and S. A. Hackney, Li_2MnO_3-stabilized $LiMO_2$ (M = Mn, Ni, Co) electrodes for lithium-ion batteries, *J. Mater. Chem.*, 2007, **17**(30), 3112–3125, DOI: 10.1039/b702425h.
43 Y.-F. Deng, S.-X. Zhao, Y.-H. Xu, K. Gao and C.-W. Nan, Impact of P-Doped in Spinel $LiNi_{0.5}Mn_{1.5}O_4$ on Degree of Disorder, Grain Morphology, and Electrochemical Performance, *Chem. Mater.*, 2015, **27**(22), 7734–7742, DOI: 10.1021/acs.chemmater.5b03517.
44 G. T.-K. Fey, C.-Z. Lu and T. P. Kumar, Preparation and electrochemical properties of high-voltage cathode materials, $LiM_yNi_{0.5-y}Mn_{1.5}O_4$ (M = Fe, Cu, Al, Mg; y = 0.0–0.4), *J. Power Sources*, 2003, **115**(2), 332–345.
45 L. Shen, H. Li, E. Uchaker, X. Zhang and G. Cao, General Strategy for Designing Core–Shell Nanostructured Materials for High-Power Lithium Ion Batteries, *Nano Lett.*, 2012, **12**(11), 5673–5678, DOI: 10.1021/nl302854j.
46 L. Wang, T. Maxisch and G. Ceder, A First-Principles Approach to Studying the Thermal Stability of Oxide Cathode Materials, *Chem. Mater.*, 2007, **19**(3), 543–552, DOI: 10.1021/cm0620943.
47 N. Yabuuchi, Y. Makimura and T. Ohzuku, Solid-State Chemistry and Electrochemistry of $LiCo_{1/3}Ni_{1/3}Mn_{1/3}O_2$ for Advanced Lithium-Ion Batteries: III. Rechargeable Capacity and Cycleability, *J. Electrochem. Soc.*, 2007, **154**(4), A314–A321.
48 N. Yabuuchi, K. Yoshii, S.-T. Myung, I. Nakai and S. Komaba, Detailed Studies of a High-Capacity Electrode Material for Rechargeable Batteries, Li_2MnO_3–$LiCo_{1/3}Ni_{1/3}Mn_{1/3}O_2$, *J. Am. Chem. Soc.*, 2011, **133**(12), 4404–4419, DOI: 10.1021/ja108588y.
49 I. Belharouak, G. M. Koenig and K. Amine, Electrochemistry and safety of $Li_4Ti_5O_{12}$ and graphite anodes paired with $LiMn_2O_4$ for hybrid electric vehicle Li-ion battery applications, *J. Power Sources*, 2011, **196**(23), 10344–10350.
50 F. Brochu, A. Guerfi, J. Trottier, M. Kopeć, A. Mauger, H. Groult, *et al.*, Structure and electrochemistry of scaling nano C–$LiFePO_4$ synthesized by hydrothermal route: complexing agent effect, *J. Power Sources*, 2012, **214**, 1–6.
51 F. Wu, M. Wang, Y. Su, L. Bao and S. Chen, A novel method for synthesis of layered $LiNi_{1/3}Mn_{1/3}Co_{1/3}O_2$ as cathode material for lithium-ion battery, *J. Power Sources*, 2010, **195**(8), 2362–2367.
52 J. Liu, R. Jiang, X. Wang, T. Huang and A. Yu, The defect chemistry of $LiFePO_4$ prepared by hydrothermal method at different pH values, *J. Power Sources*, 2009, **194**(1), 536–540.
53 F. Wu, Z. Wang, Y. Su, Y. Guan, Y. Jin, N. Yan, *et al.*, Synthesis and characterization of hollow spherical cathode $Li_{1.2}Mn_{0.54}Ni_{0.13}Co_{0.13}O_2$ assembled with nanostructured particles *via* homogeneous precipitation-hydrothermal synthesis, *J. Power Sources*, 2014, **267**, 337–346.
54 S. Deng, D. Mao, H. Wang, B. Wang, J. Liu, Y. Ma, *et al.*, Preparation and electrochemical properties of double-shell $LiNi_{0.5}Mn_{1.5}O_4$ hollow microspheres as cathode materials for Li-ion batteries, *RSC Adv.*, 2016, **6**(51), 45369–45375, DOI: 10.1039/c6ra05620b.
55 T. Doi, Y. Iriyama, T. Abe and Z. Ogumi, Electrochemical Insertion and Extraction of Lithium Ion at Uniform Nanosized $Li_{4/3}Ti_{5/3}O_4$ Particles Prepared by a Spray

Pyrolysis Method, *Chem. Mater.*, 2005, **17**(6), 1580–1582, DOI: 10.1021/cm047848x.

56 X. Huang, Y. You, Y. Ren, H. Wang, Y. Chen, X. Ding, *et al.*, Spray drying-assisted synthesis of hollow spherical Li_2FeSiO_4/C particles with high performance for Li-ion batteries, *Solid State Ionics*, 2015, **278**, 203–208.

57 T. Li, X. Li, Z. Wang, H. Guo, W. Peng and K. Zeng, Electrochemical properties of $LiNi_{0.6}Co_{0.2}Mn_{0.2}O_2$ as cathode material for Li-ion batteries prepared by ultrasonic spray pyrolysis, *Mater. Lett.*, 2015, **159**, 39–42.

58 B. Pişkin and M. K. Aydinol, Development and characterization of layered $Li(Ni_xMn_yCo_{1-x-y})O_2$ cathode materials for lithium ion batteries, *Int. J. Hydrogen Energy*, 2016, **41**(23), 9852–9859.

59 T. J. Boyle, M. A. Rodriguez, D. Ingersoll, T. J. Headley, S. D. Bunge, D. M. Pedrotty, *et al.*, A Novel Family of Structurally Characterized Lithium Cobalt Double Aryloxides and the Nanoparticles and Thin Films Generated Therefrom, *Chem. Mater.*, 2003, **15**(20), 3903–3912, DOI: 10.1021/cm020902u.

60 J. S. Park, A. U. Mane, J. W. Elam and J. R. Croy, Amorphous Metal Fluoride Passivation Coatings Prepared by Atomic Layer Deposition on $LiCoO_2$ for Li-Ion Batteries, *Chem. Mater.*, 2015, **27**(6), 1917–1920, DOI: 10.1021/acs.chemmater.5b00603.

61 J. S. Park, X. Meng, J. W. Elam, S. Hao, C. Wolverton, C. Kim, *et al.*, Ultrathin Lithium-Ion Conducting Coatings for Increased Interfacial Stability in High Voltage Lithium-Ion Batteries, *Chem. Mater.*, 2014, **26**(10), 3128–3134, DOI: 10.1021/cm500512n.

62 V. A. Sugiawati, F. Vacandio, M. Eyraud, P. Knauth and T. Djenizian, Porous NASICON-Type $Li_3Fe_2(PO_4)_3$ Thin Film Deposited by RF Sputtering as Cathode Material for Li-Ion Microbatteries, *Nanoscale Res. Lett.*, 2016, **11**(1), 365.

63 X. Zhang, F. Cheng, K. Zhang, Y. Liang, S. Yang, J. Liang, *et al.*, Facile polymer-assisted synthesis of $LiNi_{0.5}Mn_{1.5}O_4$ with a hierarchical micro–nano structure and high rate capability, *RSC Adv.*, 2012, **2**(13), 5669.

64 D. Wang, I. Belharouak, G. Zhou and K. Amine, Synthesis of Lithium and Manganese-Rich Cathode Materials *via* an Oxalate Co-Precipitation Method, *J. Electrochem. Soc.*, 2013, **160**(5), A3108–A3112, DOI: 10.1149/2.016305jes.

65 L. Zhang, W. Borong, L. Ning and W. Feng, Hierarchically porous micro-rod lithium-rich cathode material $Li_{1.2}Ni_{0.13}Mn_{0.54}Co_{0.13}O_2$ for high performance lithium-ion batteries, *Electrochim. Acta*, 2014, **118**, 67–74.

66 Z. Yang, J. Lu, D. Bian, W. Zhang, X. Yang, J. Xia, *et al.*, Stepwise co-precipitation to synthesize $LiNi_{1/3}Co_{1/3}Mn_{1/3}O_2$ one-dimensional hierarchical structure for lithium ion batteries, *J. Power Sources*, 2014, **272**, 144–151.

67 H. Liu, G. Zhu, L. Zhang, Q. Qu, M. Shen and H. Zheng, Controllable synthesis of spinel lithium nickel manganese oxide cathode material with enhanced electrochemical performances through a modified oxalate co-precipitation method, *J. Power Sources*, 2015, **274**, 1180–1187.

68 A. Huizing, H. A. M. van Hal, W. Kwestroo, C. Langereis and P. C. van Loosdregt, Hydrates of Manganese(II) Oxalate, *Mater. Res. Bull.*, 1977, **12**, 605–611.

69 R. Zhao, Z. Chen, Y. Zhang, P. Du and H. Chen, Ultrasonic/microwave-assisted co-precipitation method in the synthesis of $Li_{1.1}Mn_{0.433}Ni_{0.233}Co_{0.233}O_2$ cathode material for lithium-ion batteries, *Mater. Lett.*, 2014, **136**, 160–163.

70 L. Li, X. Zhang, R. Chen, T. Zhao, J. Lu, F. Wu, *et al.*, Synthesis and electrochemical performance of cathode material $Li_{1.2}Co_{0.13}Ni_{0.13}Mn_{0.54}O_2$ from spent lithium-ion batteries, *J. Power Sources*, 2014, **249**, 28–34.

71 A. van Bommel and J. R. Dahn, Analysis of the growth mechanism of coprecipitated spherical and dense nickel, manganese, and cobalt-containing hydroxides in the presence of aqueous ammonia, *Chem. Mater.*, 2009, **21**(8), 1500–1503.

72 K. R. Chemelewski, D. W. Shin, W. Li and A. Manthiram, Octahedral and truncated high-voltage spinel cathodes: the role of morphology and surface planes in electrochemical properties, *J. Mater. Chem. A*, 2013, **1**(10), 3347.

73 W. Luo, Effect of morphology on the physical and electrochemical properties of the high-voltage spinel cathode $LiMn_{1.5}Ni_{0.5}O_4$, *J. Alloys Compd.*, 2015, **636**, 24–28.

74 L. Wan, Y. Deng, C. Yang, H. Xu, X. Qin and G. Chen, Ni/Mn ratio and morphology-dependent crystallographic facet structure and electrochemical properties of the high-voltage spinel $LiNi_{0.5}Mn_{1.5}O_4$ cathode material, *RSC Adv.*, 2015, **5**(33), 25988–25997.

75 Y. Qian, Y. Deng, L. Wan, H. Xu, X. Qin and G. Chen, Investigation of the Effect of Extra Lithium Addition and Postannealing on the Electrochemical Performance of High-Voltage Spinel $LiNi_{0.5}Mn_{1.5}O_4$ Cathode Material, *J. Phys. Chem. C*, 2014, **118**(29), 15581–15589, DOI: 10.1021/jp503584k.

76 H. Kawai, M. Nagata, H. Tukamoto and A. R. West, High-voltage lithium cathode materials, *J. Power Sources*, 1999, **81–82**, 67–72.

77 H. B. Lin, Y. M. Zhang, H. B. Rong, S. W. Mai, J. N. Hu, Y. H. Liao, *et al.*, Crystallographic facet- and size-controllable synthesis of spinel $LiNi_{0.5}Mn_{1.5}O_4$ with excellent cyclic stability as cathode of high voltage lithium ion battery, *J. Mater. Chem. A*, 2014, **2**(30), 11987–11995, DOI: 10.1039/c4ta01810a.

78 W. Ren, R. Luo, Z. Liu, X. Tan, Z. Fu and S. Liao, Effect of Ni/Mn ratio on the performance of $LiNi_xMn_{2-x}O_4$ cathode material for lithium-ion battery, *Ionics*, 2014, **20**(10), 1361–1366, DOI: 10.1007/s11581-014-1114-3.

79 K. Amine, H. Tukamoto, H. Yasuda and Y. Fujita, Preparation and electrochemical investigation of $LiMn_{2-x}Me_xO_4$ (Me: Ni, Fe, and $x = 0.5, 1$) cathode materials for secondary lithium batteries, *J. Power Sources*, 1997, **68**(2), 604–608.

80 J. Fan, G. Li, D. Luo, C. Fu, Q. Li, J. Zheng, *et al.*, Hydrothermal-Assisted Synthesis of Li-Rich Layered Oxide Microspheres with High Capacity and Superior Rate-

capability as a Cathode for Lithium-ion Batteries, *Electrochim. Acta*, 2015, **173**, 7–16.

81 H. Groult, T. Nakajima and N. Kumagai, Characterization and Electrochemical Properties of $LiNi_{0.5}Mn_{1.5}O_4$ Prepared by a Carbonate Co-Precipitation Method, *Int. J. Electrochem. Sci.*, 2014, **9**, 7712–7724.

82 G. M. Koenig, I. Belharouak, H. M. Wu and K. Amine, Hollow lithiated metal oxide particles as lithium-ion battery cathode materials, *Electrochim. Acta*, 2011, **56**(3), 1426–1431.

83 G. M. Koenig, I. Belharouak, H. Deng, Y.-K. Sun and K. Amine, Composition-Tailored Synthesis of Gradient Transition Metal Precursor Particles for Lithium-Ion Battery Cathode Materials, *Chem. Mater.*, 2011 Apr 12, **23**(7), 1954–1963, DOI: 10.1021/cm200058c.

84 D. Wang, I. Belharouak, G. M. Koenig, G. Zhou and K. Amine, Growth mechanism of $Ni_{0.3}Mn_{0.7}CO_3$ precursor for high capacity Li-ion battery cathodes, *J. Mater. Chem.*, 2011, **21**(25), 9290.

85 Z. Zheng, X. Guo, S. Chou, W. Hua and H. Liu, Electrochimica Acta Designed Synthesis and Their Improved Electrochemical Performance, *Electrochim. Acta*, 2016, **191**, 401–410, DOI: 10.1016/j.electacta.2016.01.092.

86 S. Zhang, C. Deng, B. L. Fu, S. Y. Yang and L. Ma, Synthetic optimization of spherical $Li[Ni_{1/3}Mn_{1/3}Co_{1/3}]O_2$ prepared by a carbonate co-precipitation method, *Powder Technol.*, 2010, **198**(3), 373–380.

87 L. Li, S. Song, X. Zhang, R. Chen, J. Lu, F. Wu, *et al.*, Ultrasonic-assisted co-precipitation to synthesize lithium-rich cathode $Li_{1.3}Ni_{0.21}Mn_{0.64}O_2$ + d materials for lithium-ion batteries, *J. Power Sources*, 2014, **272**, 922–928.

88 M. Noh and J. Cho, Optimized Synthetic Conditions of $LiNi_{0.5}Co_{0.2}Mn_{0.3}O_2$ Cathode Materials for High Rate Lithium Batteries *via* Co-Precipitation Method, *J. Electrochem. Soc.*, 2013, **160**(1), A105–A111.

89 H. Xie, G. Hu, K. Du, Z. Peng and Y. Cao, An improved continuous co-precipitation method to synthesize $LiNi_{0.80}Co_{0.15}Al_{0.05}O_2$ cathode material, *J. Alloys Compd.*, 2016, 84–87.

90 H. Wang, X.-Z. Liao, Y. Yang, X. Yan, Y.-S. He and Z.-F. Ma, Large-Scale Synthesis of $NaNi_{1/3}Fe_{1/3}Mn_{1/3}O_2$ as High Performance Cathode Materials for Sodium Ion Batteries, *J. Electrochem. Soc.*, 2016, **163**(3), A565–A570.

91 G. B. Liu, H. Liu and Y. F. Shi, Electrochimica Acta The synthesis and electrochemical properties of $xLi_2MnO_{3-(1-x)}MO_2$ (M = $Mn_{1/3}Ni_{1/3}$ $Fe_{1/3}$) *via* co-precipitation method, *Electrochim. Acta*, 2013, **88**, 112–116, DOI: 10.1016/j.electacta.2012.10.054.

92 A. Angermann and J. Töpfer, Synthesis of nanocrystalline Mn–Zn ferrite powders through thermolysis of mixed oxalates, *Ceram. Int.*, 2011, **37**(3), 995–1002.

93 U. García-Couceiro, O. Castillo, A. Luque, G. Beobide and P. Román, A new hydrated phase of cobalt(II) oxalate: crystal structure, thermal behavior and magnetic properties of $\{[Co_{(\mu-ox)}(H_2O)_2]\cdot 2H_2O\}_n$, *Inorg. Chim. Acta*, 2004, **357**(1), 339–344.

94 M. C. López, J. L. Tirado and C. Pérez Vicente, Structural and comparative electrochemical study of M(II) oxalates, M = Mn, Fe, Co, Ni, Cu, Zn, *J. Power Sources*, 2013, **227**, 65–71.

95 S. Guillemet-Fritsch, M. Aoun-Habbache, J. Sarrias, A. Rousset, N. Jongen, M. Donnet, *et al.*, High-quality nickel manganese oxalate powders synthesized in a new segmented flow tubular reactor, *Solid State Ionics*, 2004, **171**(1–2), 135–140.

96 P. Axmann, G. Gabrielli and M. Wohlfahrt-Mehrens, Tailoring high-voltage and high-performance $LiNi_{0.5}Mn_{1.5}O_4$ cathode material for high energy lithium-ion batteries, *J. Power Sources*, 2016, **301**, 151–159.

97 F. Cheng, Y. Xin, J. Chen, L. Lu, X. Zhang and H. Zhou, Monodisperse $Li_{1.2}Mn_{0.6}Ni_{0.2}O_2$ microspheres with enhanced lithium storage capability, *J. Mater. Chem. A*, 2013, **1**(17), 5301.

98 J. C. Arrebola, A. Caballero, M. Cruz, L. Hernán, J. Morales and E. R. Castellón, Crystallinity Control of a Nanostructured $LiNi_{0.5}Mn_{1.5}O_4$ Spinel *via* Polymer-Assisted Synthesis: A Method for Improving Its Rate Capability and Performance in 5 V Lithium Batteries, *Adv. Funct. Mater.*, 2006, **16**(14), 1904–1912, DOI: 10.1002/adfm.200500892.

99 Z. Qin, X. Zhou, Y. Xia, C. Tang and Z. Liu, Morphology controlled synthesis and modification of high-performance $LiMnPO_4$ cathode materials for Li-ion batteries, *J. Mater. Chem.*, 2012, **22**(39), 21144.

100 J. Zhang, X. Guo, S. Yao, W. Zhu and X. Qiu, Tailored synthesis of $Ni_{0.25}Mn_{0.75}CO_3$ spherical precursors for high capacity Li-rich cathode materials *via* a urea-based precipitation method, *J. Power Sources*, 2013, **238**, 245–250.

101 J. P. Robinson and G. M. Koenig, Tuning solution chemistry for morphology control of lithium-ion battery precursor particles, *Powder Technol.*, 2015, **284**, 225–230.

102 D. G. Wickham, SOLID-PHASE EQUILIBRIA IN THE SYSTEM NiO-Mn_2O_3-O_2, *J. Inorg. Nucl. Chem.*, 1964, **26**, 1369–1377.

103 J. Vázquez, P. L. López-Alemany, P. Villares and R. Jiménez-Garay, A theoretical study on the crystallized fraction and the kinetic parameters by continuous heating techniques. Application to the devitrification of the $Sb_{0.16}As_{0.36}Se_{0.48}$ alloy, *Mater. Lett.*, 1998, **35**(1), 50–57.

104 M. E. Brown and A. K. Galwey, Thermal Decomposition of Manganese(II) Oxalate in Vacuum and in Oxygen, *J. Chem. Soc., Faraday Trans. 1*, 1974, **70**, 1316–1324.

105 N. Mancilla, V. Caliva, M. C. D'Antonio, A. C. González-Baró and E. J. Baran, Vibrational spectroscopic investigation of the hydrates of manganese(II) oxalate, *J. Raman Spectrosc.*, 2009, **40**(8), 915–920, DOI: 10.1002/jrs.2200.

106 J. Topfer and J. Jung, Thermal decomposition of mixed crystals $Ni_xMn_{3-x}(C_2O_4)_3\cdot 6H_2O$, *Thermochim. Acta*, 1992, **202**, 281–289.

107 D. B. Wiles and R. A. Young, A new computer program for Rietveld analysis of X-ray powder diffraction patterns, *J. Appl. Crystallogr.*, 1981, **14**(2), 149–151, DOI: 10.1107/S0021889881008996.

108 A. Feltz, J. Töpfer and F. Schirrmeister, Conductivity data and preparation routes for $NiMn_2O_4$ thermistor ceramics, *J. Eur. Ceram. Soc.*, 1992, **9**(3), 187–191.

109 J. Song, D. W. Shin, Y. Lu, C. D. Amos, A. Manthiram and J. B. Goodenough, Role of Oxygen Vacancies on the Performance of $Li[Ni_{0.5-x}Mn_{1.5+x}]O_4$ ($x = 0$, 0.05, and 0.08) Spinel Cathodes for Lithium-Ion Batteries, *Chem. Mater.*, 2012, **24**, 3101–3109.

110 W. W. Wu, H. F. Xiang, G. B. Zhong, W. Su, W. Tang, Y. Zhang, *et al.*, Ordered $LiNi_{0.5}Mn_{1.5}O_4$ hollow microspheres as high-rate 5 V cathode materials for lithium ion batteries, *Electrochim. Acta*, 2014, **119**, 206–213.

111 M. M. Thackeray, Lithiated Oxides for Lithium Ion Batteries, *J. Electrochem. Soc.*, 1995, **142**(8), 2558–2563.

112 K. Dokko, M. Mohamedi, N. Anzue, T. Itoh and I. Uchida, In situ Raman spectroscopic studies of $LiNi_xMn_{2-x}O_4$ thin film cathode materials for lithium ion secondary batteries, *J. Mater. Chem.*, 2002, **12**(12), 3688–3693.

113 Q. Zhong, A. Bonakclarpour, M. Zhang, Y. Gao and J. R. Dahn, Synthesis and Electrochemistry of $LiNi_xMn_{2-x}O_4$, *J. Electrochem. Soc.*, 1997, **144**(1), 205–213, DOI: 10.1149/1.1837386.

114 W. Tang, Y. Hou, F. Wang, L. Liu, Y. Wu and K. Zhu, $LiMn_2O_4$ nanotube as cathode material of second-level charge capability for aqueous rechargeable batteries, *Nano Lett.*, 2013, **13**(5), 2036–2040.

115 J. S. Kim, K. Kim, W. Cho, W. H. Shin, R. Kanno and J. W. Choi, A truncated manganese spinel cathode for excellent power and lifetime in lithium-ion batteries, *Nano Lett.*, 2012, **12**(12), 6358–6365.

116 Y.-C. Jin and J.-G. Duh, Nanostructured $LiNi_{0.5}Mn_{1.5}O_4$ cathode material synthesized by polymer-assisted co-precipitation method with improved rate capability, *Mater. Lett.*, 2013, **93**, 77–80.

117 S.-K. Hong, S.-I. Mho, I.-H. Yeo, Y. Kang and D.-W. Kim, Structural and electrochemical characteristics of morphology-controlled $Li[Ni_{0.5}Mn_{1.5}]O_4$ cathodes, *Electrochim. Acta*, 2015, **156**, 29–37.

118 W. Shao, S. Chen, L. He, H. Li, X. Guo and H. Zhu, *et al.*, Electrochemical performances discharged to lower potential for co-precipitation method, *5th Int Conf Inf Eng Mech Mater*, 2015.

119 J. G. Speight and N. A. Lange, *Lange's handbook of chemistry*, McGraw-Hill Professional, Maidenhead, 2005.